

Lunar regolith thermal gradients and emission spectra: Modeling and validation

L. Millán,^{1,2} I. Thomas,¹ and N. Bowles¹

Received 25 May 2011; revised 28 September 2011; accepted 29 September 2011; published 15 December 2011.

[1] The retrieval of surface composition from IR measurements of airless bodies requires a model capable of computing the significant thermal gradients present in the top few hundred microns of the regolith. In this study we introduce a model which reproduces most of the features found in controlled experiments made in the simulated lunar environment emission chamber (SLEEC). Although the model presented here is forced by a lower boundary held at a fixed temperature, we conclude that a similar algorithm driven by solar illumination may be used as a forward model to retrieve composition, particle size and effective thermal conductivity from IR measurements of airless bodies.

Citation: Millán, L., I. Thomas, and N. Bowles (2011), Lunar regolith thermal gradients and emission spectra: Modeling and validation, *J. Geophys. Res.*, 116, E12003, doi:10.1029/2011JE003874.

1. Introduction

[2] Planetary surfaces emit thermal infrared radiation as a function of their composition, grain size distribution, temperature and surface roughness. Depending on the wavelength and the opacity of the surface, this thermal infrared radiation originates at different depths and the overall intensity of the emitted radiation at the surface is a combination of these different “emission layers.” To properly interpret measurements under such conditions, the temperature distribution in the upper layers of the regolith in question needs to be accurately modeled.

[3] As discussed by *Henderson and Jakosky* [1994, 1997], on planetary bodies with a substantial atmosphere such as the Earth, this modeling is not necessary because the interstitial gas between the particles of the regolith effectively redistribute the heat (by increasing the thermal convection). As a result the temperature distribution of these layers is practically isothermal. However, on airless bodies such as the Moon, the lack of interstitial gas reduces the thermal conductivity and, if the temperature of the medium is sufficiently high, thermal radiation can dominate the heat transport in the top few millimeters of the surface creating a thermal gradient due to the thermal radiation to space.

[4] As measured by *Logan and Hunt* [1970], *Logan et al.* [1973], and *Henderson et al.* [1996] and modeled by *Henderson and Jakosky* [1994, 1997], these thermal gradients alter the emission spectrum. One of the most notable changes is the shift of the location of the Christiansen feature (CF). The CF occurs where the real part of the refractive index is equal to that of the surrounding medium [*Conel*, 1969] causing a minimum in scattering and hence a

maximum in transmission. As pointed out by *Conel* [1969] and fully recognized by *Salisbury and Walter* [1989], this shifting can be used as a diagnostic of composition.

[5] The Lunar Diviner Radiometer Experiment (Diviner), launched in June 2009 on-board of NASA’s Lunar Reconnaissance Orbiter, is the first lunar orbiting radiometer capable of measuring the lunar CF spectral region with its three narrow channels located near 8 μm (7.55–8.05 μm , 8.10–8.40 μm and 8.36–8.68 μm) [*Paige et al.*, 2009]. Fully interpreting these measured spectra requires a model capable of reproducing the spectral emissivity behavior on the Moon.

[6] In this paper we model a slab of material in equilibrium with a lower boundary held at a fixed temperature. Although in reality the Moon is heated from the top by solar illumination, this configuration allows us to compare the modeled results against experimental data from the simulated lunar environment emission chamber (SLEEC) (I. Thomas et al., manuscript in preparation, 2011). We show that this thermal model reproduces reasonably well the experimental data suggesting that a similar model (one driven by solar illumination) may be used as forward model to invert the mineralogy information contained in the global emission data from the 8 μm channels of the Diviner instrument.

2. Model Description

[7] The physical model presented here is based on the model described by *Henderson and Jakosky* [1994] but with the use of an alternative, and in principal more accurate, radiative transfer scheme (DISORT [*Stamnes et al.*, 1988]) and a MIE scattering code derived from atmospheric scattering calculations (Thomas, G. and D. Grainger, (2011), Oxford University MIE code, available from www.atm.ox.ac.uk/code/mie/). The formalism of this model follows that used by *Henderson and Jakosky* [1994] and is summarized below. Note that *Henderson and Jakosky* [1997] updated their first model to include scattering, but its sample is driven only by incident sunlight which complicates its validation against laboratory measurements.

¹Clarendon Laboratory, Atmospheric, Oceanic and Planetary Physics, University of Oxford, Oxford, UK.

²Now at Jet Propulsion Laboratory, California Institute of Technology, Pasadena, California, USA.

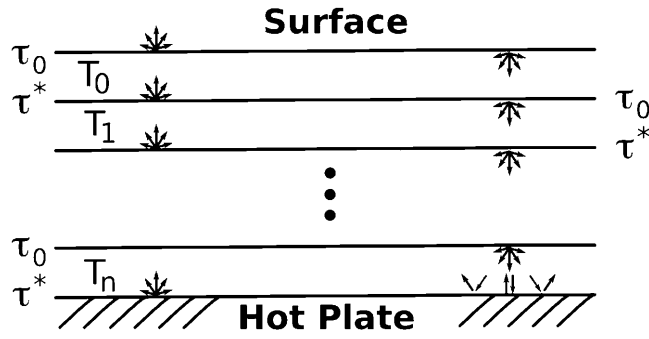


Figure 1. Schematic illustration of a medium divided into layers of equal optical thickness driven by reflection and thermal emission at the bottom boundary. Each layer is described by a single temperature.

[8] The model here presented is a numerical solution of a semi-infinite, horizontally stratified particulated medium in equilibrium with a lower boundary held at fixed temperature (see Figure 1). Starting from an isothermal temperature, in a time step fashion, the model computes the heating rate between the layers, allowing the medium to equilibrate its temperature. The steady state temperature is then used to compute an emission spectrum which can be compared with laboratory measurements.

[9] In this study, the heat transfer mechanisms are grouped into two categories: the radiative and the nonradiative contributions. The nonradiative heat transfer contributions are calculated using the Fourier's law of heat conduction,

$$q = -k_e \frac{dT}{dz} \quad (1)$$

where q is the heat flux, dT/dz is the temperature gradient in the z -direction which is measured downward from the surface and where k_e is the effective thermal conductivity given by,

$$k_e = k_s + k_g \quad (2)$$

in which k_s and k_g represent the heat conduction through direct contact of the particles and the heat convection through the interstitial gas (i.e. the solid and the gas portion of the thermal conductivity) respectively. It should be noted that for airless bodies such as the Moon there is no gas to carry the heat through convection, and hence k_g will be zero. Furthermore, under such conditions, the model is required to force the heat conduction to be zero at the interface between the medium and the space environment since there is no medium to conduct the thermal energy, that is to say,

$$k_e \frac{dT}{dz} = 0 \quad (3)$$

at the immediate, top, surface.

[10] The nonradiative heating rate will be given by,

$$h_c = -\frac{d}{dz}(-q) \quad (4)$$

which needs to be added with the radiative heating rate to compute the temperature change after a single time step.

[11] The radiative heating transfer contributions are computed using formal radiative transfer theory as described by Chandrasekhar [1960] and Thomas and Stamnes [1999]. At the core of this theory is the equation of radiative transfer describing the propagation of radiation through an absorbing, emitting and scattering medium. The fundamental assumption of this equation is that the constituent particles of the medium do not interact coherently (i.e. all the elements of the regolith behave independently). Although one would expect this assumption to be false in a close packed medium such as a regolith, Hapke [1993] has argued that since the particles are randomly positioned, the oriented coherent effects should be negligible. Furthermore, Conel [1969] and Moersch and Christensen [1995] have demonstrated that models based on the radiative transfer equation successfully reproduce many of the features seen in the thermal emission spectra of powder.

[12] The general radiation transfer equation (at given wave number ν) is (after Chandrasekhar [1960] and Thomas and Stamnes [1999]),

$$\mu \frac{dI_\nu(\tau_\nu, \Omega)}{d\tau_\nu} = -I_\nu(\tau_\nu, \Omega) + S_\nu(\tau_\nu, \Omega) \quad (5)$$

where I_ν is the spectral radiance, τ_ν is the extinction optical depth, Ω the direction of travel of the radiation, μ is the cosine of the angle between Ω and the surface normal and S_ν is the source function due to thermal emission and multiple scattering given by,

$$S_\nu(\tau_\nu, \Omega) = [1 - a_\nu(\tau_\nu)]B_\nu(\tau_\nu) + \frac{a_\nu(\tau_\nu)}{4\pi} \cdot \int_{4\pi} d\omega' p_\nu(\tau_\nu, \Omega', \Omega) I_\nu(\tau_\nu, \Omega') \quad (6)$$

where a_ν is the single scattering albedo, B_ν is the Planck function, ω is the solid angle and p_ν is the scattering phase function.

[13] In a slab geometry, the solutions for the upward ($^+$) and downward ($^-$) intensities are,

$$I_\nu^+(\tau_\nu, \mu, \phi) = I_\nu^+(\tau_\nu^*, \mu, \phi) \exp^{-(\tau_\nu^* - \tau_\nu)/\mu} + \int_{\tau_\nu}^{\tau_\nu^*} \frac{d\tau'_\nu}{\mu} S_\nu(\tau'_\nu, \mu, \phi) \exp^{-(\tau'_\nu - \tau_\nu)/\mu} \quad (7)$$

$$I_\nu^-(\tau_\nu, \mu, \phi) = I_\nu^-(0, \mu, \phi) \exp^{(-\tau_\nu/\mu)} + \int_0^{\tau_\nu} \frac{d\tau'_\nu}{\mu} S_\nu(\tau'_\nu, \mu, \phi) \exp^{-(\tau_\nu - \tau'_\nu)/\mu} \quad (8)$$

where ϕ is the azimuthal angle and where the optical depth is measured downward from the top of the medium ($\tau_\nu = 0$) to the bottom ($\tau_\nu = \tau_\nu^*$).

[14] The associate radiative fluxes are,

$$F_\nu^+(\tau_\nu) = \int_0^{2\pi} d\phi \int_0^1 I_\nu^+ 2\pi\mu d\mu \quad (9)$$

$$F_\nu^-(\tau_\nu) = \int_0^{2\pi} d\phi \int_0^1 I_\nu^- 2\pi\mu d\mu \quad (10)$$

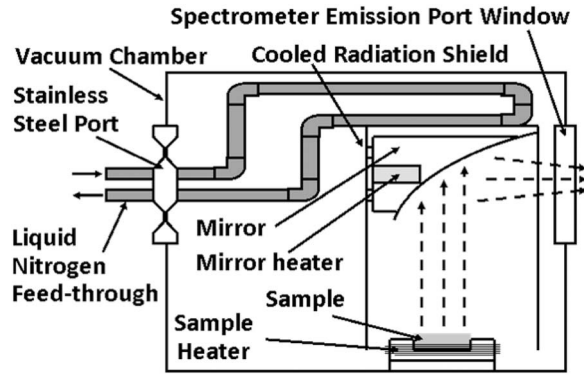


Figure 2. Schematic representation of the Simulated Lunar Environment Emission Chamber (Thomas et al., manuscript in preparation, 2011).

which are related to the radiative heat flux through the radiative heating rate h_r ,

$$h_r = - \int_0^\infty d\nu \frac{\partial F_\nu}{\partial z} \quad (11)$$

where F_ν is the radiative flux in the z direction determined by $F_\nu^+ - F_\nu^-$.

[15] In the experimental setup simulated in this work, at the interface between the sample and the hot plate, the upward flux is given by the Stefan–Boltzmann law,

$$F_\nu^+(\tau_\nu^p) = \sigma T_p^4 \quad (12)$$

where σ is the Boltzmann constant and T_p is the temperature of the hot plate, while the upward intensity will be given by,

$$I_\nu^+(\tau_\nu^p, \mu, \phi) = B_\nu(T_p) + r I_\nu^-(\tau_\nu^p, \mu, \phi) \quad (13)$$

where τ_ν^p is the optical depth at the plate and where r is the reflectivity of the plate.

[16] Combining the radiative and the nonradiative heating rates, the temperature change for each layer after a single step time is,

$$\frac{dT}{dt} = \frac{h_r + h_c}{\rho C} \quad (14)$$

where ρ and C are the density and the heat capacity of the material.

[17] This whole process is repeated until the temperature of the medium reaches a steady state. At this stage, this final temperature is used to track the upward intensity leaving the hot plate through the layers of the sample to compute the radiation field escaping the medium.

[18] This model was implemented using two well tested, publicly available codes. The Mie code subroutines developed at Oxford University (Thomas, G. and D. Grainger, (2011), Oxford University MIE code, available from www.atm.ox.ac.uk/code/mie/) were used to compute all the radiative transfer parameters needed (i.e. τ_ν , a_ν , p_ν). These

subroutines were run either assuming a single particle distribution or a lognormal distribution. The lognormal distribution is described by,

$$n(r) = \frac{N_0}{2\pi} \frac{1}{\log(\zeta)} \frac{1}{r} \exp\left(-\frac{(\log(r) - \log(r_m))^2}{2\log^2(\zeta)}\right) \quad (15)$$

where $n(r)$ is the number density of particles as a function of the radius r , N_0 is the total number of particles, r_m is the median particle radius of the size distribution, and where ζ is the spread of the distribution where the standard deviation of $\log(r)$ is equal to $\log(\zeta)$ (that is to say, $\sigma(\log(r)) = \log(\zeta)$).

[19] N_0 is estimated using,

$$N_0 = \frac{\vartheta}{(4\pi r_m^3)/3} \quad (16)$$

where ϑ is the packing fraction.

[20] The other subroutine used was the plane-parallel, multiple scattering, radiative transfer code DISORT [Stamnes et al., 1988]. This code was used to compute the radiative fluxes as well as the final upward intensity. DISORT was run using four streams (i.e. four computational polar angles) and 16 streams to compute the radiative fluxes and intensities, respectively, as recommended by K. Stamnes et al. (*DISORT Report 1.1*, DISORT, a general-purpose Fortran program for discrete-ordinate-method radiative transfer in scattering and emitting layered media: Documentation of methodology, 2000, 107 pp., available at [ftp://climate1.gsfc.nasa.gov/wiscombe/Multiple_Scatt/DISORTReport1.1.pdf](http://climate1.gsfc.nasa.gov/wiscombe/Multiple_Scatt/DISORTReport1.1.pdf)) to ensure accurate values.

[21] When computing the thermal gradient, the steady state was reached when the mean temperature change “ dT/dt ” for all layers did not change more than 0.01% than the mean value from the previous time step.

3. Experimental Data

[22] Laboratory emission spectra used in this study were measured using the Simulated Lunar Environment Chamber (SLEEC) designed and operated by the Planetary Experiments Group at Oxford University (Thomas et al., manuscript in preparation, 2011). This emission chamber was designed to replicate lunar surface and near surface thermal environmental conditions by generating similar thermal gradients in the sample as might be found on the lunar surface.

[23] Figure 2 shows a schematic of the experiment: a 3 mm-thick sample sat in an aluminum holder which was heated up to a temperature of 500 K. The sample was surrounded by a radiation shield which was cooled through a liquid nitrogen feed allowing the background temperature to drop until 100 K. Inside this cooled radiation shield, a mirror was used to redirect the emission toward the spectrometer port. This mirror/sample/cold shield arrangement was then housed inside a vacuum chamber with the capability of maintaining internal atmospheric pressures below 10^{-3} mbar. Emission from the sample was measured by a Bruker IFS-66v Fourier transform spectrometer, equipped with a potassium bromide (KBr) emission port window,

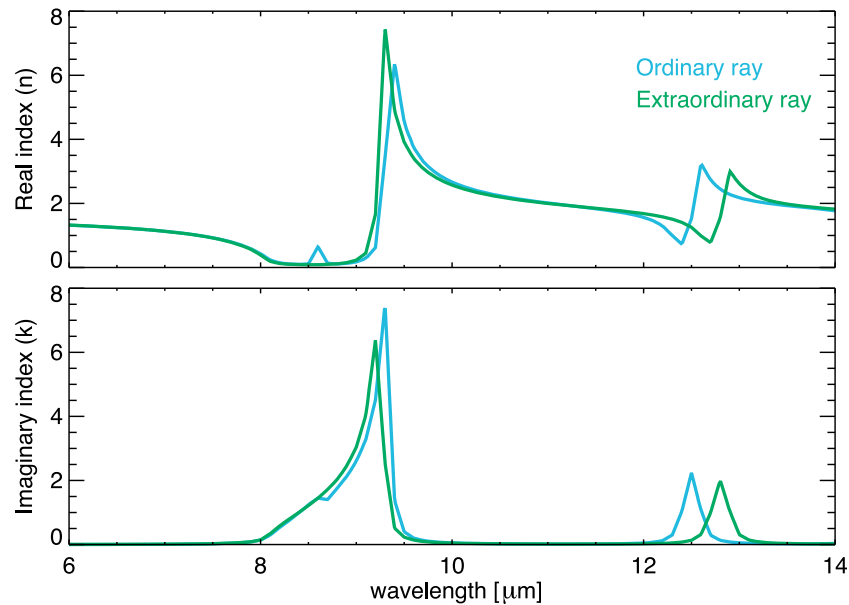


Figure 3. Real n and imaginary k refractive index of quartz for the ordinary and extraordinary ray from *Spitzer and Kleinman* [1961]. Note that around 9 and 13 μm the O-ray and E-ray differ significantly.

KBr beamsplitter and DLaTGS (deuterated L-alanine doped triglycine sulfate) detector. Under this configuration, spectra was taken from 300 to 7000 cm^{-1} (approximately from 2 to 33 μm) with a 2 cm^{-1} resolution.

[24] For this study, emission spectra were recorded for the following two experimental conditions:

[25] 1. “Half vacuum”: the temperature of the heating plate was maintained at 343 K while the background temperature was 302 K and the internal atmospheric pressure was 7 mbar.

[26] 2. Lunar-like: the temperature of the heating plate was maintained at 500 K while the background temperature was cooled to around 108 K and the internal atmospheric pressure was pumped to 10^{-4} mbar.

[27] The half vacuum conditions are representative of the Martian surface pressure where thermal gradients will not be significant and therefore will induce only minor spectral differences. Meanwhile, under lunar-like conditions the thermal gradients can alter the spectral contrast and shift the position of the Christiansen feature [*Henderson and Jakosky*, 1994, 1997].

[28] The mineral used in this study was a quartz sample with particles radius smaller than 30 μm with an unknown distribution. Although a quartz regolith is not expected to occur in nature, it was chosen because its optical constants are well known, and in order to be consistent with previous studies [*Conel*, 1969; *Moersch and Christensen*, 1995].

[29] The sample used in this study was prepared by *Greenhagen* [2009] in the following manner: High purity crystals were crushed using a combination of mortar/pestle and shatterbox to create a mineral sample with the appropriate size distribution. The mineral powders were dry sieved using disposable meshes. The sieving utilized automated sieve shakers with run times of at least 4 hours. Then, the sample was loaded into the sample holder and baked in a

vacuum oven at 50°C for at least three hours to remove water vapor and other volatile contaminants.

4. Model Inputs

[31] The model here introduced was setup and run to allow direct comparison with the SLEEC experimental data. In addition to the particle size distribution and the temperature boundary conditions, this model requires several other user supplied parameters and these are described in detail below.

4.1. Optical Constants

[32] The refractive index for quartz was taken from *Spitzer and Kleinman* [1961]. Since quartz has an anisotropic structure, to properly represent its birefringence (see Figure 3, especially around 12 μm) behavior, the usual 1/3–2/3 approximation was used, where 1/3 of the quartz grains were modeled using the parallel dielectric constant (extraordinary ray) while the other 2/3 of the sample were modeled using the perpendicular dielectric constant (ordinary ray). The validity of this approximation has been discussed by *Draine* [1988] and *Draine and Malhotra* [1993], and its effects will be shown in section 5.1.

4.2. Wavelength Range

[33] The wavelength range used in this study to compute the radiative fluxes was from 2 to 50 μm , which according to *Henderson and Jakosky* [1994] is sufficient to cover the bulk of the Planck function for most planetary surface temperatures. These fluxes were computed with a spectral resolution of 0.5 μm which was found to be a reasonable resolution that compromises the accuracy of the thermal gradient and its computing time.

[34] The upward intensity computation was restricted to the regime from 6 to 14 μm to be consistent with previous studies [*Henderson and Jakosky*, 1994, 1997; *Moersch and*

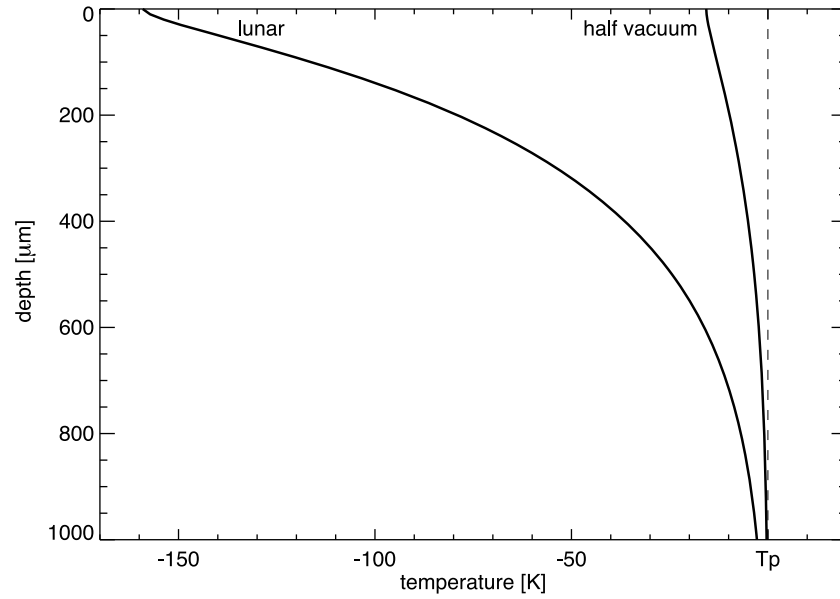


Figure 4. Computed thermal gradients in a 15 μm quartz regolith heated from below for the half vacuum and lunar-like experimental conditions (see section 3 for exact values). The thermal gradients are shown with respect to the temperature of the hot plate (T_p) for each of the simulations.

Christensen, 1995] and also because it covers the CF region (sample for compositional studies by the Diviner instrument). This intensity was computed with a spectral resolution of about 0.015 μm (the exact resolution was set to be 2 cm^{-1} to match the resolution of the new SLEEC chamber).

4.3. Lower Boundary Conditions

[35] The hot plate temperature was set to be 343 and 500 K for the half vacuum and the lunar-like conditions respectively. The reflectivity of the hot plate was set to be 0.4 (the measured reflectivity of the SLEEC heater plate).

4.4. Thermal Conductivity Values

[36] Thermal conductivity values, k_e , for evacuated and partially evacuated materials can be found in the work of Wechsler and Glaser [1965], Fountain and West [1970], and Wechsler et al. [1972]. In order to be consistent with Henderson and Jakosky [1994, 1997] for the half vacuum conditions (appropriate conditions for particulate materials on Mars) k_e was $2 \times 10^{-5}\text{ cal}/(\text{cm s K})$ while for the lunar-like conditions k_e was $1 \times 10^{-6}\text{ cal}/(\text{cm s K})$ unless clearly specified.

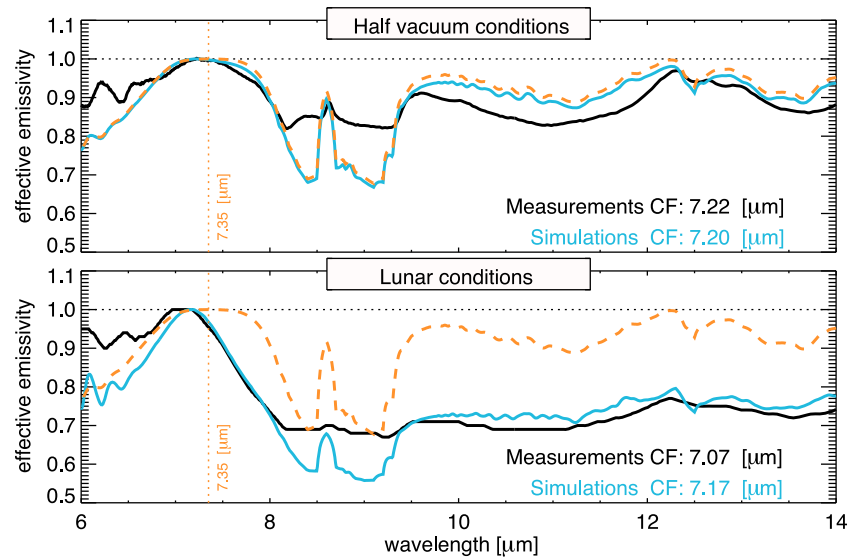


Figure 5. Simulated effective emissivity spectra of a 15 μm quartz sample heated from the base. The thermal gradients used are shown in Figure 4. Measurements from SLEEC (black solid line) along with simulations for an isothermal case (orange dashed line) are shown for comparison. The vertical line at 7.35 μm shows the isothermal position of the Christiansen frequency.

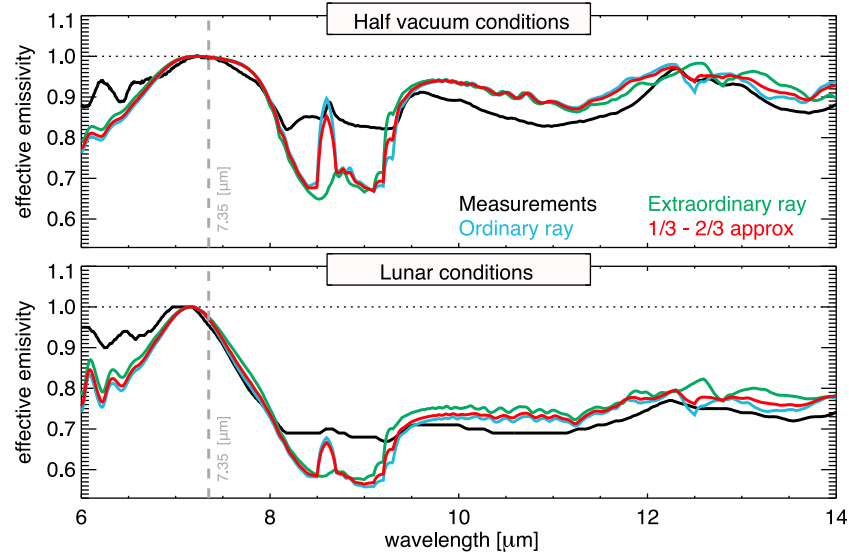


Figure 6. Simulated effective emissivity spectra of 15 μm quartz samples using the ordinary ray, the extraordinary ray, and the 1/3-2/3 approximation (blue, green and red lines, respectively). These samples were heated from the base assuming half vacuum and lunar-like conditions (see section 3 for exact values). Measurements from SLEEC (black solid line) are shown for comparison. The vertical line at 7.35 μm shows the isothermal position of the Christiansen frequency.

4.5. Other Parameters

[37] The particle size used will be varied along the simulations, in general a 15 μm grain size will be assumed, when this is not the case it will be clearly specified.

[38] The packing fraction (PF) used to compute the number of particles (as specified by equation (16)) was 0.63 which is the mean PF between a sample assuming an atomic cubic crystal structure (PF = 0.52) and a hexagonal close-packed structure (PF = 0.74). The remaining uncertainty in

this parameter (± 0.11) does not alter the results presented in this study.

5. Results

[39] Figure 4 shows the estimated thermal gradients for a 15 μm quartz regolith under half vacuum and lunar-like conditions. These simulations were done using the optical constants for the ordinary ray. As expected, the thermal gradient under half vacuum conditions is practically

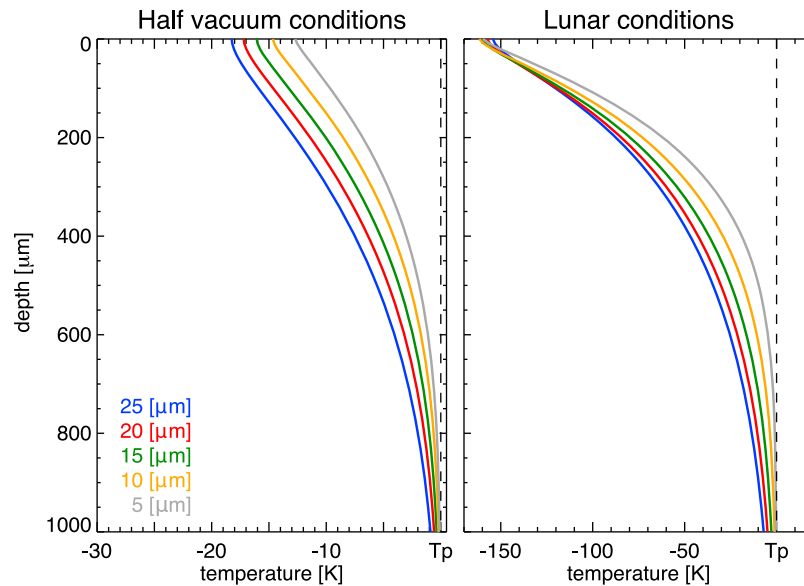


Figure 7. Computed thermal gradients for quartz regoliths with several single particle size distributions (color coded as specified in the figure). These samples were heated from below for the half vacuum and lunar-like experimental conditions (see section 3 for exact values). The thermal gradients are shown with respect to the temperature of the hot plate (T_p) for each of the simulations.

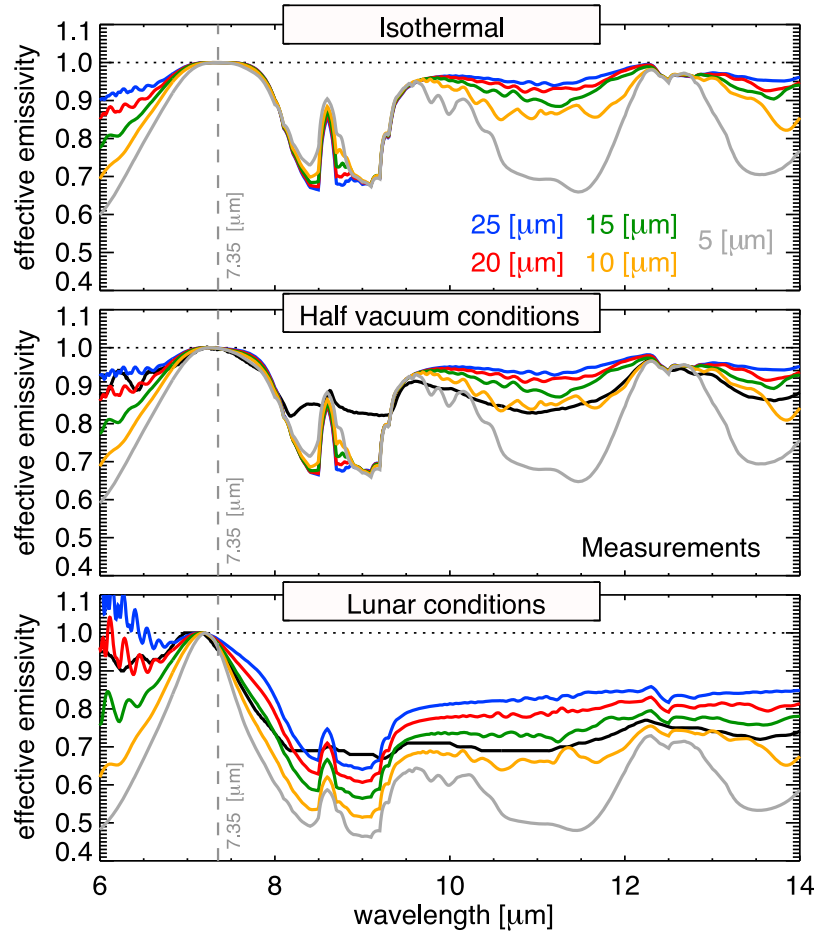


Figure 8. Simulated effective emissivity spectra of quartz samples with several single particle size distributions (color coded as specified in the figure). These samples were heated from the base assuming half vacuum and lunar-like conditions (see section 3 for exact values). The thermal gradients used are shown in Figure 7. Measurements from SLEEC (black solid line) along with simulations for an isothermal case are shown for comparison. The vertical line at $7.35 \mu\text{m}$ shows the position of the Christiansen frequency.

negligible being less than 7 K in the top $700 \mu\text{m}$ while under lunar-like conditions the temperature gradient is vast, dropping approximately 150 K in the top $1000 \mu\text{m}$.

[40] Figure 5 shows the effective emissivity spectra computed using the thermal gradients shown in Figure 4. This effective emissivity spectra, ϵ_ν was calculated assuming the Kirchhoff's law,

$$\epsilon_\nu = \frac{I_\nu}{B_\nu(T_b)} \quad (17)$$

where I_ν is the intensity escaping from the regolith at steady state, B_ν is the plank function and T_b is the maximum brightness temperature in the CF region. Figure 5 also shows the emissivity as derived from the SLEEC measurements for comparison. The spectra measured was converted to emissivity using a method similar to the one described by *Christensen and Harrison* [1993], adapted to cope with the large thermal gradients within the sample.

[41] To demonstrate the effect of the presence of the thermal gradient on the spectral shape, the results were compared with simulations for an isothermal quartz regolith. In this case, the CF is located at $7.35 \mu\text{m}$ followed by the

Reststrahlen band (RB) region located approximately between 8 and $14 \mu\text{m}$.

[42] As can be seen under half vacuum and lunar-like conditions, the location of the CF was shifted to 7.20 and $7.17 \mu\text{m}$ respectively. These shifts do not completely agree with the measurement-derived CF locations (7.22 and $7.07 \mu\text{m}$) suggesting that a different combination of input parameters is needed to better fit the experimental data; however, these shifts do show the expected behavior with a greater shift for the lunar-like conditions.

[43] With respect to the RBs, there are two features to notice. The first one is that under both experimental conditions there is a considerable discrepancy around $8.5 \mu\text{m}$. The reason for this discrepancy is still unknown but it is probable that the sample holder is emitting some radiation thus reducing the spectral contrast in this region. In addition, this discrepancy might be related to the fact that Mie theory only applies to isolated spherical particles, while the sample is closely-packed and the grain shapes are irregular. To investigate if this is the case, more experiments are required, but the model provides a starting point to investigate them further. For instance, implementing methods to deal with close packing conditions such as the ones described by *Wald*

Table 1. CF Location for the Emissivity Spectra Shown in Figure 8

Radius (μm)	Half Vacuum CF (μm)	Lunar-Like CF (μm)
Measurements	7.22	7.07
25	7.20	6.53
20	7.20	7.15
15	7.21	7.17
10	7.23	7.20
5	7.28	7.20

[1994] and *Mishchenko* [1994] and giving a more realistic treatment to the particle shape.

[44] The second feature to notice is that under lunar-like conditions the intensity of the RB has decreased simply because its radiation arises near the surface where (due to the pronounced thermal gradient) the temperature is considerably colder than deeper where the radiation of the CF comes from.

[45] The following sections explore the different model parameters that can be varied in order to find a better fit against the experimental data.

5.1. The Effect of the Quartz Birefringence

[46] Figure 6 displays the simulated emissivity spectra of a 15 μm quartz regolith using the optical constants of the ordinary ray, the extraordinary ray, and using the 1/3–2/3 approximation for each experimental condition. The thermal gradients computed using the extraordinary ray and the 1/3–2/3 approximation are not shown because they were exactly the same as the thermal gradients computed for the ordinary ray (shown in Figure 4). This implies that the heat transfer in the sample was the same regardless of the optical constants used. Hence, the CF locations for all half vacuum and all lunar-like cases are the same as the ones found in Figure 5 (7.20 and 7.17 μm for half vacuum and lunar-like conditions respectively).

[47] The most noticeable consequence of using the 1/3–2/3 approximation can be found around 12 μm where the ordinary ray and the extraordinary ray refractive index differ the most. As can be seen in Figure 6 (especially in the half vacuum case), the 1/3–2/3 approximation improves the similarity between the measurements and the simulations reproducing the three consecutive local maxima in the region.

[48] Note that since the 1/3–2/3 approximation better represents the measurements, it will be used for the rest of the simulations presented in this study.

5.2. The Effect of Varying the Particle Size

[49] Figure 7 shows the temperature gradients modeled for several single particle size quartz regoliths for each experimental condition. As can be seen, in general, the thermal gradient increases with increasing particle size. At first sight, this result may appear contrary to that found by *Presley and Christensen* [1997] where thermal gradients were found to decrease with increasing particle size, however, these two results arise from two different scenarios. In the measurements performed by *Presley and Christensen* [1997] when the particle size varied, the thermal conductivity of the sample and the radiative and scattering properties of the medium were changing. On the other hand, in the simulations

presented here, the thermal conductivity was constrained to either 2×10^{-5} or 1×10^{-6} cal/(cm s K) depending on which experimental conditions were modeled irrespective of the particle size. Therefore, in our simulations, varying the particle size was only changing the radiative and scattering properties of the medium.

[50] Figure 8 shows the effective emissivity spectra computed for the quartz regoliths modeled in Figure 7. In these comparisons, there are two effects that need to be separated: (1) the change in the emissivity due to the different scattering properties associated to each particle size and (2) the change in the emissivity due to the different thermal gradients (including the shift of the CF).

[51] The first effect can be isolated by simulating the emissivity spectra for the different particle size distributions under isothermal conditions. As the particle size decreases, the CF width gets narrower, the spectral contrast in the RB increases and the RB intensity decreases. These simulations agree with the results of *Salisbury et al.* [1987] (note that their conclusions are for reflectance spectra).

[52] A mixture of the first and second effect can be appreciated distinctively under lunar-like conditions. On top of the changes due to the different scattering properties, as the particle size increases, the CF shifts toward smaller wavelengths. Furthermore, the intensity of the RB spreads more than the variation shown in the isothermal case.

[53] An analysis of the positions of the CF locations in Table 1 implies two contradictory conclusions: for the half vacuum condition the simulations suggest that the mean particle size of the sample might lie between 15 and 10 μm while for the lunar-like conditions the CF locations suggest that the mean particle size of the sample might lie between 20 and 25 μm . These results indicate that in order to consistently match the measurements, other parameters need to be taken in consideration.

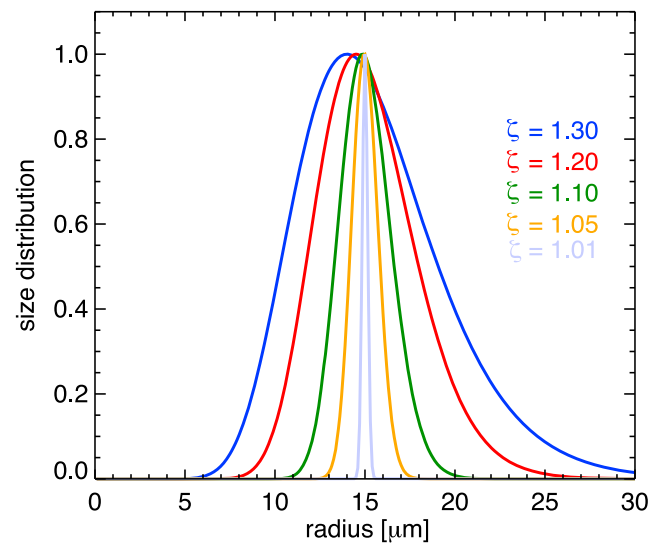


Figure 9. Lognormal particle size distributions used to investigate the effects of the spread of the particle size distribution. The mean radius is 15 μm and the different spread values, ζ in equation (15), are color coded.

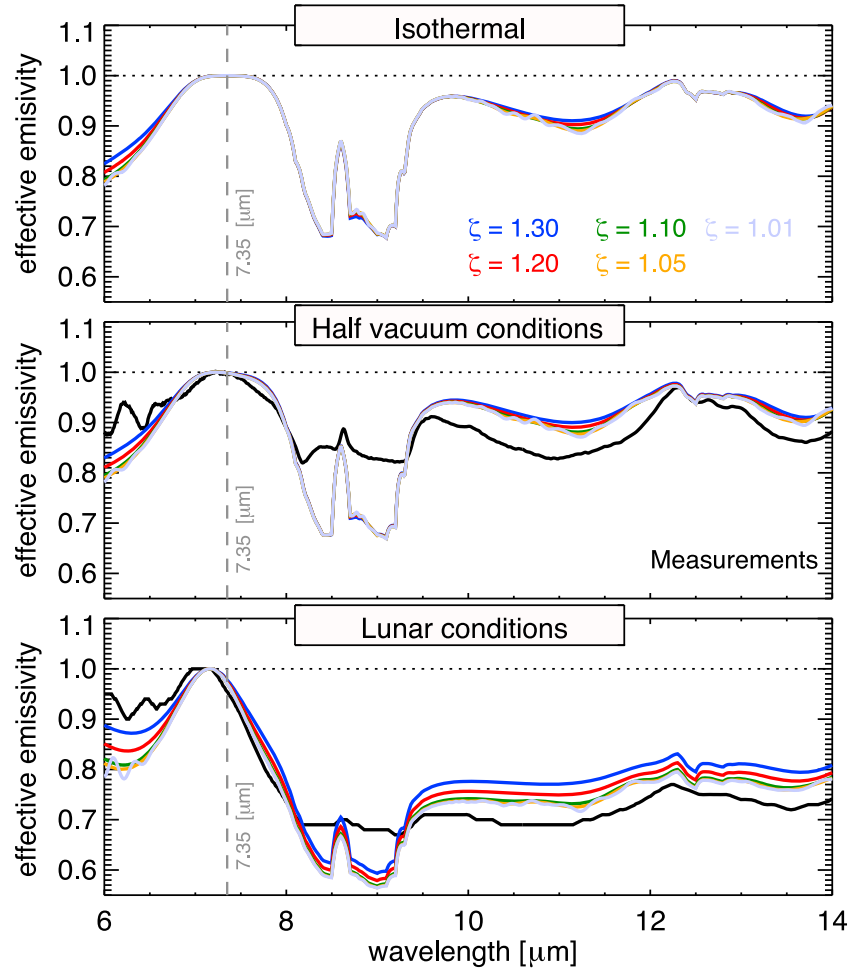


Figure 10. Simulated effective emissivity spectra of quartz samples with the lognormal particle size distributions (color coded as specified in the figure) shown in Figure 9. These samples were heated from the base assuming half vacuum and lunar-like experimental conditions (see section 3 for exact values). Measurements from SLEEC (black solid line) along with simulations for an isothermal case are shown for comparison. The vertical line at $7.35 \mu\text{m}$ shows the isothermal position of the Christiansen frequency.

5.3. The Effect of Varying the Particle Distribution

[54] To investigate the effect of changing the spread of the particle size distribution in the simulations, the lognormal distributions shown in Figure 9 were used to compute their corresponding thermal gradients and the effective emissivity spectra (see Figure 10).

[55] The thermal gradients for each experimental condition are nearly identical to those shown in Figure 4, mainly because the mean radius of the particle size distributions is $15 \mu\text{m}$. Hence, as should be expected, the CF locations for all the half vacuum simulations were $7.20 \mu\text{m}$ while all the lunar-like simulations were $7.17 \mu\text{m}$, just as before.

[56] The most noticeable consequence of changing the spread of the distribution is that as the spread of the distribution widens, the effective emissivity spectra smooths out.

5.4. The Effect of Varying the Thermal Conductivity

[57] Figure 11 shows the temperature gradients modeled for a $15 \mu\text{m}$ quartz regolith with several values of k_e . For half vacuum conditions k_e was set to 2×10^{-5} , 1×10^{-5} and $5 \times 10^{-6} \text{ cal}/(\text{cm s K})$ while for lunar-like conditions k_e was

set to 1×10^{-6} , 5×10^{-7} , and $2.5 \times 10^{-7} \text{ cal}/(\text{cm s K})$. As expected, the thermal gradients steepen as k_e decrease.

[58] Figure 12 shows the effective emissivity spectra for all these simulated regoliths along with the measurement-derived emissivity for comparison. Their corresponding CF locations can be found in Table 2. These CF locations, in addition to those shown in Table 1, suggest that in order to better fit the measurements, a proper combination of the thermal conductivity and the particle size of the distribution is needed.

6. Summary and Discussion

[59] In this study we introduce a radiative and thermal conductive heat transfer model of a regolith in equilibrium with a lower boundary held at a fixed temperature and compare it against measurements from an emission chamber designed to replicate different space environments such as the lunar and the Mars (half vacuum) conditions. Starting from an isothermal temperature distribution, the model divides the regolith in layers of equal optical depth and tracks the heat flux exchange between the layers which

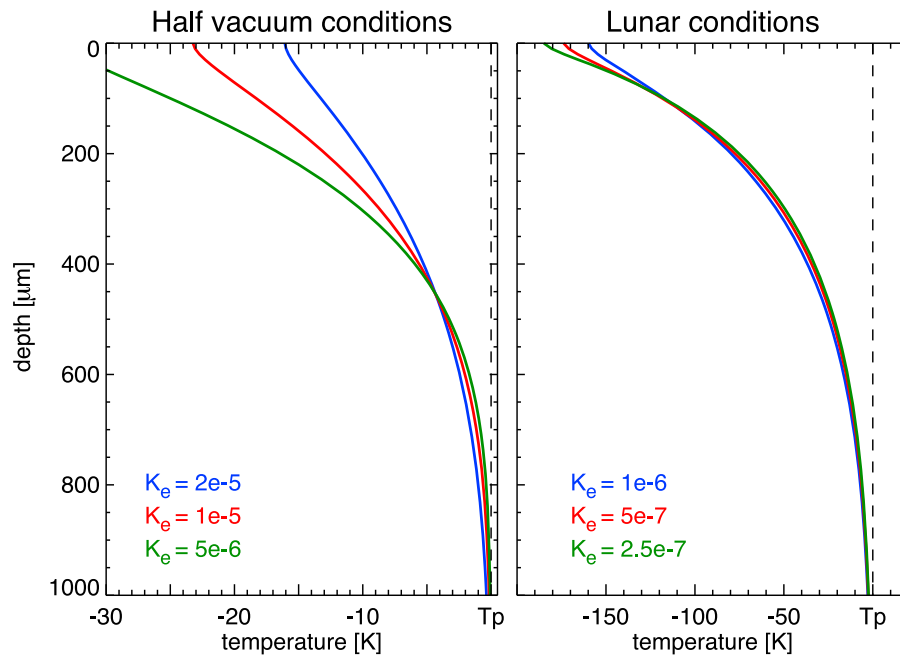


Figure 11. Computed thermal gradients for 15 μm quartz regoliths heated from below assuming several conductivity values (color coded as specified in the figure) for the half vacuum ($T_p = 343$ K) and lunar-like conditions ($T_p = 500$ K). The thermal gradients are shown with respect to the temperature of the hot plate (T_p) for each of the simulations.

varies according to the user-supplied model inputs (particle size distribution, refractive index, thermal conductivity, and temperature of the lower boundary). Once the steady state is reached, the model uses the temperature distribution to

compute the intensity leaving the regolith and an effective emissivity spectrum.

[60] The results shown here reproduce well the features displayed in the measured data, such as the spectral shift of

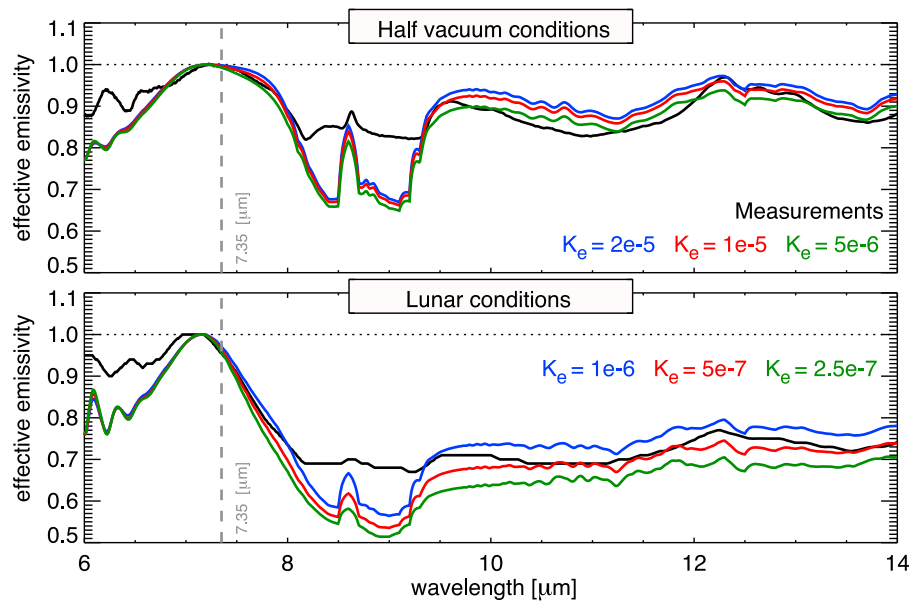


Figure 12. Simulated effective emissivity spectra of 15 μm quartz samples. These samples were heated from the base assuming several conductivity values (color coded as specified in the figure) for the half vacuum ($T_p = 343$ K) and lunar-like conditions ($T_p = 500$ K). The thermal gradients used are shown in Figure 11. Measurements from SLEEC (black solid line) are shown for comparison. The vertical line at 7.35 μm shows the isothermal position of the Christiansen frequency.

Table 2. CF Location for the Emissivity Spectra Shown in Figure 12

k_e (cal/(cm s K))	Half Vacuum CF (μm)	k_e (cal/(cm s K))	Lunar-Like CF (μm)
Measurements	7.22	Measurements	7.07
2e-5	7.21	1e-6	7.17
1e-5	7.19	5e-7	7.16
5e-6	7.19	2.5e-7	7.14

the CF, the decrease of the effective emissivity intensity of the RB region under lunar-like thermal conditions, and the three local maxima near 12 μm due to the birefringence of quartz. This strongly suggests that the modeled thermal gradients represent the thermal distribution in the measured sample and that this problem can be approached using Mie theory despite being theoretically only for isolated spherical particles.

[61] In conclusion, a similar model, currently under development, driven by solar illumination rather than by a lower boundary held at a fixed temperature can be used as a forward model to attempt the retrieval of composition, particle size distribution, and thermal conductivity from IR measurements of airless bodies such as those made by the Diviner instrument. The effects of topography and space weathering will need to be addressed when those algorithms are developed.

[62] **Acknowledgments.** We thank G. Thomas and M. Munro for their help with setting up and running DISORT and the Oxford Mie code. This research was carried out in part at the University of Oxford and at the Jet Propulsion Laboratory, California Institute of Technology, under a contract with NASA. This work was supported by the UK Science and Technology Facilities Council and the Diviner Lunar Radiometer Experiment science budget.

References

- Chandrasekhar, S. (1960), *Radiative Transfer*, Dover, New York.
- Christensen, P. R., and S. T. Harrison (1993), Thermal infrared emission spectroscopy of natural surfaces: Application to desert varnish coatings on rocks, *Astrophys. J.*, 414, 632–645.
- Conel, J. E. (1969), Infrared emissivities of silicates: Experimental results and a cloudy atmosphere model of spectral emission from condensed particulate mediums, *J. Geophys. Res.*, 74(6), 1614–1634.
- Draine, B. T. (1988), The discrete-dipole approximation and its application to interstellar graphite grains, *Astrophys. J.*, 333, 848–872.
- Draine, B. T., and S. Malhotra (1993), On graphite and the 2175 Å extinction profile, *Astrophys. J.*, 414, 632–645.
- Fountain, J. A., and E. A. West (1970), Thermal conductivity of particulate basalt as a function of density in simulated lunar and Martian environments, *J. Geophys. Res.*, 75(20), 4063–4069.
- Greenhagen, B. T. (2009), Thermal emission remote sensing of the Moon: Design and development of Diviner lunar radiometer compositional capabilities, Ph.D. thesis, Dept. of Earth and Space Sci., Univ. of Calif., Los Angeles.
- Hapke, B. (1993), *Theory of Reflectance and Emittance Spectroscopy*, Cambridge Univ. Press, Cambridge, U. K.
- Henderson, B. G., and B. M. Jakosky (1994), Near-surface thermal gradients and their effects on midinfrared emission spectra of planetary surfaces, *J. Geophys. Res.*, 99(E9), 19,063–19,073.
- Henderson, B. G., and B. M. Jakosky (1997), Near surface thermal gradients and mid-IR emission spectra: A new model including scattering and application to real data, *J. Geophys. Res.*, 102(E3), 6567–6580.
- Henderson, B. G., P. G. Lucey, and B. M. Jakosky (1996), New laboratory measurements of mid-IR emission spectra of simulated planetary surfaces, *J. Geophys. Res.*, 101(E6), 14,969–14,975.
- Logan, L. M., and G. R. Hunt (1970), Emission spectra of particulate silicates under simulated lunar conditions, *J. Geophys. Res.*, 75(32), 6539–6548.
- Logan, L. M., G. R. Hunt, J. W. Salisbury, and S. R. Balsamo (1973), Composition implications of Christiansen frequency maximums for infrared remote sensing applications, *J. Geophys. Res.*, 78(23), 4983–5003.
- Mishchenko M. I. (1994), Asymmetry parameters of the phase function for densely packed scattering grains, *J. Quant. Spectrosc. Radiat. Transfer*, 52(1), 95–110.
- Moersch, J. E., and P. R. Christensen (1995), Thermal emission from particulate surfaces: A comparison of scattering models with measured spectra, *J. Geophys. Res.*, 100(E4), 7465–7477.
- Paige, D. A., et al. (2009), The Lunar Reconnaissance Orbiter Diviner Lunar Radiometer Experiment, *Space Sci. Rev.*, 150, 125–160.
- Presley, M. A., and P. R. Christensen (1997), Thermal conductivity measurements of particulate materials: 2. Results, *J. Geophys. Res.*, 102(E3), 6551–6566.
- Salisbury, J., and L. S. Walter (1989), Thermal infrared (2.5–13.5 μm) spectroscopic remote sensing of igneous rock types on particulate planetary surfaces, *J. Geophys. Res.*, 94(B7), 9192–9202.
- Salisbury, J., B. Hapke, and J. Estes (1987), Usefulness of weak bands in midinfrared remote sensing of particulate planetary surfaces, *J. Geophys. Res.*, 92(B1), 702–710.
- Spitzer, W. G., and D. A. Kleinman (1961), Infrared lattice bands of quartz, *Phys. Rev.*, 121(5), 1324–1335.
- Stamnes, K., S. C. Tsay, W. Wiscombe, and K. Jayaweera (1988), A numerically stable algorithm for discrete-ordinate-method radiative transfer in multiple scattering and emitting layered media, *Appl. Opt.*, 27, 2502–2509.
- Thomas, G. E., and K. Stamnes (1999), *Radiative Transfer in the Atmosphere and Ocean*, Cambridge Univ. Press, Cambridge, U. K.
- Wald, A. E. (1994), Modeling thermal infrared (2–14 μm) reflectance spectra of frost and snow, *J. Geophys. Res.*, 99(B12), 24,241–24,250.
- Wechsler, A. E., and P. E. Glaser (1965), Pressure effects on postulated lunar materials, *Icarus*, 4, 335–352.
- Wechsler, A. E., P. E. Glaser, and J. A. Fountain (1972), Thermal properties of granulated materials, in *Thermal Characteristics of the Moon*, edited by J. W. Lucas, pp. 215–241, MIT Press, Cambridge, Mass.
- N. Bowles and I. Thomas, Clarendon Laboratory, Atmospheric, Oceanic and Planetary Physics, University of Oxford, Parks Road, Oxford OX1 3PU, UK.
- L. Millán, Jet Propulsion Laboratory, California Institute of Technology, 4800 Oak Grove Dr., Pasadena, CA 91109–8099, USA. (lmillan@jpl.nasa.gov)